J. Fluid Mech. (2003), *vol.* 490, *pp.* 15–35.
DOI: 10.1017/S0022112003005184 Printed in the United Kingdom

On self-propulsion of micro-machines at low Reynolds number: Purcell's three-link swimmer

By L. E. BECKER[1], S. A. KOEHLER[2]† AND H. A. STONE[2]

[1]BLF Consulting, 18 Washington Avenue, Toronto, Ontario, M5S 1L2, Canada

[2]Division of Engineering & Applied Sciences, Harvard University, Cambridge, MA 02138, USA

(Received 13 August 2002 and in revised form 13 August 2002)

Using slender-body hydrodynamics in the inertialess limit, we examine the motion of Purcell's swimmer, a planar, fore–aft-symmetric three-link flagellum or propulsive mechanism that translates by alternately moving its front and rear segments. Purcell (1976) concluded via symmetry arguments that the net displacement of such a swimmer must follow a straight line, but the direction and other details of the motion have never been investigated. Numerical results indicate that the direction of net translation and the speed of Purcell's swimmer depend on the angular amplitude of the swimming strokes as well as on the relative length of the links. Analytical results are presented for small rotations about the straightened configuration, and physical arguments are given to qualitatively explain the propulsive dynamics. The optimal swimmer configurations under the conditions of constant forcing and of minimum mechanical work are determined. We use a definition of efficiency based on the straightened configuration as a reference state to compare Purcell's swimmer with the previously treated swimming motions of an undulating rod and a rotating helix. Finally, we demonstrate the importance of the anisotropy in the local hydrodynamic slender-body drag to swimming motions at low Reynolds number by showing that, in general, any inextensible swimmer in an otherwise quiescent fluid cannot alter its average position under conditions of locally isotropic drag.

1. Introduction

The vast majority of organisms on Earth are microscopic in size, and they propel themselves through liquid in a manner that is fundamentally different from that of larger creatures such as mammals or fish, which gain forward momentum after having pushed back on the surrounding fluid. For very small bodies, however, as elegantly described by G. I. Taylor in the movie *Low Reynolds Number Flows*, inertial forces are typically negligible in comparison to viscous drag, so that the Reynolds number characterizing the flow is much less than one. In the inertialess limit, the Navier–Stokes equations may be linearized, and hence reciprocal motions such as the opening and closing of the 'scallop', the singly hinged rigid swimmer shown in figure 1(*a*), do not result in any net translation or rotation (Happel & Brenner 1965; Childress 1981). In the well-known discussion by Purcell (1976) on "Life at Low Reynolds Number", he presents a description of the 'simplest animal' that can swim under these conditions: the two-hinged swimmer depicted in figure 1(*b*). Purcell

† Present address: Department of Physics, Emory University, Atlanta, GA 30322-2430, USA.

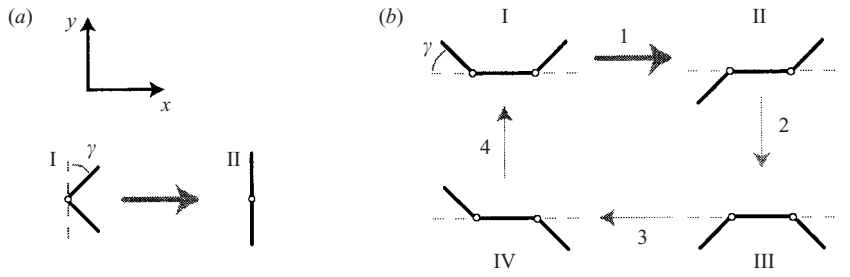

FIGURE 1. Simple configuration sequences for two hypothetical swimmers restricted to the (x, y)-plane: (a) the "scallop", which has a single joint that is depicted opening with stroke angle γ to the straightened position, and (b)"Purcell's swimmer", which alternately rotates its two arms until the angle between them and the middle link equals $\pm\gamma$.

indicated that a fore–aft-symmetric linkage with two hinges (three links) would move in a straight line over one cycle of alternately moving its front and rear links, but the details of this motion were not investigated. Indeed the direction of motion was left as an exercise to the reader, but after more than two decades there still does not appear to be a satisfactory answer to that question (Castaing 1998). In this paper, we provide a detailed study of this simplest of hypothetical low-Reynolds-number swimmers that are inextensible with rotating joints.

There exists considerable interest in studying the propulsive mechanics of common micro-organisms such as spermatozoa (e.g. Keller & Rubinow 1976*a*) and algae (e.g. Pedley & Kessler 1987) as well as their macroscopic collective dynamics (e.g. Hill, Pedley & Kessler 1989). Although the swimming strategies observed in nature are typically more complicated than that of Purcell's swimmer treated herein, a recent conjecture by Berg (2002) proposes that small helical bacteria called Spiroplasmas might propel themselves in a manner similar to Purcell's swimmer but with non-parallel axes of bending for the two idealized joints. Furthermore, recent advances in micro-machines raise the possibility of deploying self-propelled micro-robots inside the human body for minimally invasive therapeutic treatments (Iddan *et al.* 2000; Ishiyama *et al.* 2001*a*, *b*). The simplicity of Purcell's swimmer may therefore prove practical in the design of micro-robots in addition to representing a useful model to explore fundamental aspects of self-propulsion at low Reynolds numbers.

Early research on the planar motion of organisms at low Reynolds number considered the propagation of plane waves along sheets and rods (e.g. Taylor 1951; Hancock 1953; Lighthill 1975), while more recent investigations have focused on the propulsion produced by wave-like disturbances travelling along elastic filaments (e.g. Wiggins & Goldstein 1998; Camalet, Jülicher & Prost 1999) and along surfaces of non-slender bodies (e.g. Blake 1971; Shapere & Wilczek 1989*a*, *b*; Stone & Samuel 1996; Ajdari & Stone 1999). Studies of non-planar motions of organisms have been confined mainly to the propulsion of a helix rotating about its axis (e.g. Phan-Thien, Tran-Cong & Ramia 1987; Lighthill 1996; Purcell 1997), with some recent theoretical work on over-twisted elastica and their relation to experimentally observed super-coiled filaments (plectonemes) produced by the bacterium *B. subtilis* (Goldstein, Powers & Wiggins 1998; Koehler & Powers 2000). Many of these existing models of swimming micro-organisms assume that the filament is infinitely long, that the amplitude of the shape perturbations is small, or that the idealized propulsive element is acted upon by some external force/torque. Conversely, given the inherent geometric simplicity of Purcell's swimmer, it is possible to model the large-amplitude motion of a physically

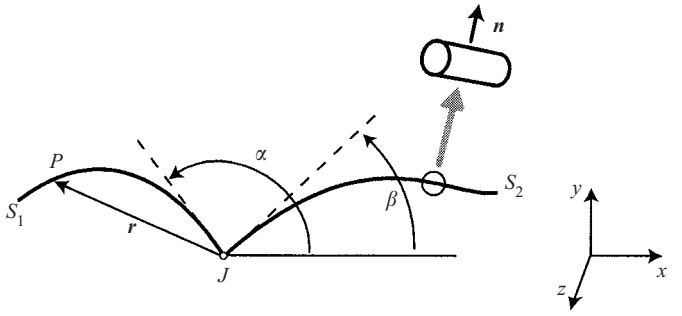

FIGURE 2. A general, singly jointed swimmer, where surfaces/links S_1 and S_2 move as rigid bodies. The swimmer and its motion are confined to the (x, y)-plane.

realizable force-free linkage of slender bodies driven by internal motors acting at the joints, as well as to determine the optimal swimmer for a given set of conditions.

In § 2, we use the linearity of the equations for the inertialess limit to derive the equations governing the motion of a rigid linkage with only one mobile joint. These equations plus symmetry arguments are applied in § 3 to investigate the detailed motion of Purcell's swimmer. In § 4, we determine the optimal swimming configurations for Purcell's swimmer under the conditions of constant forcing and minimum mechanical work. We also propose a new efficiency criterion to compare Purcell's swimmer to the undulating rod and the rotating helix. Finally, to demonstrate the importance of the anisotropy of the local fluid drag to swimming motions, we give a simple proof that any inextensible swimmer in an otherwise quiescent fluid cannot swim under isotropic drag, a condition where the local hydrodynamic force per unit length acting on the linkage is taken as directly proportional to the local fluid velocity. Our conclusions are summarized in § 5.

2. Single-joint dynamics

We begin our study of micro-mechanical self-propulsion by examining the planar one-joint slender linkage shown in figure 2. Without loss of generality, we only consider motion in the (x, y)-plane. The velocity $\boldsymbol{U}_P$ of any point P on the single-joint linkage, relative to the fixed, inertial, Cartesian frame depicted in figure 2, may be decomposed into three components: the velocity due to a translation of the joint J, the velocity due to a rigid-body rotation about J, and the velocity due to a symmetric 'stretching motion':

$$\boldsymbol{U}_P = \begin{cases} \boldsymbol{U}_J + \boldsymbol{\Omega} \wedge \boldsymbol{r} + \boldsymbol{\omega} \wedge \boldsymbol{r} & \text{on } S_1 \\ \boldsymbol{U}_J + \boldsymbol{\Omega} \wedge \boldsymbol{r} - \boldsymbol{\omega} \wedge \boldsymbol{r} & \text{on } S_2, \end{cases} \tag{1}$$

where $\boldsymbol{r}$ is the position vector from the joint J to point P, $\boldsymbol{U}_J$ is the velocity of the joint, and the angular velocities $\boldsymbol{\Omega}$ and $\boldsymbol{\omega}$ are related to the time derivatives of the angles α and β defined in figure 2 by

$$\boldsymbol{\Omega} = \left(\frac{\dot{\alpha} + \dot{\beta}}{2}\right)\boldsymbol{e}_z, \quad \boldsymbol{\omega} = \left(\frac{\dot{\alpha} - \dot{\beta}}{2}\right)\boldsymbol{e}_z, \tag{2}$$

where $\boldsymbol{e}_z$ is a unit vector in the z-direction. We wish to solve the continuity and Stokes equations,

$$\nabla \cdot \boldsymbol{u} = 0, \tag{3a}$$

$$\nabla \cdot \boldsymbol{\sigma} = -\nabla p + \mu \nabla^2 \boldsymbol{u} = \boldsymbol{0}, \tag{3b}$$

for the slender linkage in an otherwise quiescent fluid, where $(\boldsymbol{u}, p, \boldsymbol{\sigma})$ are the velocity, pressure, and stress fields, respectively. In the absence of externally applied force fields, the swimmer overall is force- and torque-free. Motion is effected via equal but opposing moments between the two links, which are considered to move as rigid bodies. From elementary force and torque balances, with elimination of the force of constraint at the common joint J, a natural choice of generalized forces corresponding to the generalized velocities $\boldsymbol{U}_J$, $\boldsymbol{\Omega}$ and $\boldsymbol{\omega}$ is the total force $\boldsymbol{F}$ $(=\boldsymbol{0})$, the total moment $\boldsymbol{L}$ $(=\boldsymbol{0})$ about J, and the torque difference between the links acting at J and driving the motion of the swimmer. More specifically, the linearity of the governing equations implies the following relation valid for arbitrarily shaped single-jointed objects (and generalizable in a straightforward fashion to an arbitrary number of joints):

$$\begin{pmatrix} \boldsymbol{R}_{FU} & \boldsymbol{R}_{F\Omega} & \boldsymbol{R}_{F\omega} \\ \boldsymbol{R}_{LU} & \boldsymbol{R}_{L\Omega} & \boldsymbol{R}_{L\omega} \\ \boldsymbol{R}_{SU} & \boldsymbol{R}_{S\Omega} & \boldsymbol{R}_{S\omega} \end{pmatrix} \begin{bmatrix} \boldsymbol{U}_J \\ \boldsymbol{\Omega} \\ \boldsymbol{\omega} \end{bmatrix} = \begin{bmatrix} \boldsymbol{F} = \int_{S_P} \boldsymbol{n}\cdot\boldsymbol{\sigma}\,\mathrm{d}S \\ \boldsymbol{L} = \int_{S_P} \boldsymbol{r}\wedge(\boldsymbol{n}\cdot\boldsymbol{\sigma})\,\mathrm{d}S \\ \boldsymbol{S} = \int_{S_1} \boldsymbol{r}\wedge(\boldsymbol{n}\cdot\boldsymbol{\sigma})\,\mathrm{d}S - \int_{S_2} \boldsymbol{r}\wedge(\boldsymbol{n}\cdot\boldsymbol{\sigma})\,\mathrm{d}S \end{bmatrix} = \begin{bmatrix} \boldsymbol{0} \\ \boldsymbol{0} \\ -\boldsymbol{S}^{ext} \end{bmatrix}, \tag{4}$$

where the unit normal vector $\boldsymbol{n}$ of the (finite-thickness) links is directed into the fluid. Here $\boldsymbol{S}^{ext} \equiv -\boldsymbol{S} = S^{ext}\boldsymbol{e}_z$ is the torque difference or 'strain forcing' that the mechanism in the (x, y)-plane applies to the surrounding fluid, and represents the external torque applied to link S_1 minus that on link S_2. This strain forcing of the motion may be thought of as resulting from a rubber band stretched across the active joint, or alternatively as twice the torque exerted by one side on the other via a motor, for example.

The grand resistance matrix on the left-hand side of equation (4) may be shown to be overall symmetric via the reciprocal theorem (Hinch 1972), so that, for example, $\boldsymbol{R}_{FU} = \boldsymbol{R}_{FU}^T$ and $\boldsymbol{R}_{F\Omega} = \boldsymbol{R}_{LU}^T$. The individual resistance matrices of equation (4) depend on the viscosity, size, and instantaneous configuration of the object, and thus uniquely determine the quantities $\boldsymbol{U}_J$, $\boldsymbol{\Omega}$, and $\boldsymbol{\omega}$; here they will be computed according to (4) using the leading-order slender-body approximation (Batchelor 1970), which gives for example that

$$\int_{\Gamma(s)} \boldsymbol{n}\cdot\boldsymbol{\sigma}\,\mathrm{d}\Gamma = -\left[\frac{2\pi\mu}{\ln(2/\epsilon)}\right](2\boldsymbol{I} - \boldsymbol{\lambda}\boldsymbol{\lambda})\cdot\boldsymbol{U}(s) + O[\ln^{-2}(2/\epsilon)], \tag{5}$$

where s denotes arclength along the centreline, $\Gamma(s)$ the circumference of the cross-section, μ the viscosity, ϵ the slenderness ratio of link diameter to its length, $\boldsymbol{\lambda}$ the unit tangent vector to the body, $[2\pi\mu/\ln(2/\epsilon)] \equiv \zeta$ represents an effective resistance coefficient, and $\boldsymbol{U}(s)$ is the local velocity of the linkage. For example, with respect to a Cartesian reference frame, the first column of the sub-matrix $\boldsymbol{R}_{FU}$ in the planar case contains the $\{x, y\}$ components of the total hydrodynamic force exerted on the linkage as a result of a pure rigid-body translation with unit velocity in the x-direction. All components of the grand resistance matrix are determined similarly by individually assigning unit velocities to the non-trivial components of $\boldsymbol{U}_J, \boldsymbol{\Omega}$, and $\boldsymbol{\omega}$, a process which, for motion in the (x,y)-plane, reduces the governing matrix equation (4) to a 4×4 system of equations, linear in the four unknown scalar velocities $(\boldsymbol{U}_J)_x$, $(\boldsymbol{U}_J)_y$, $\Omega \equiv \boldsymbol{\Omega}_z$, and $\omega \equiv \boldsymbol{\omega}_z$.

As indicated in equation (5), the error involved in applying the leading-order slender-body approximation to obtain an effective force density (per unit length) along the centreline is $O[\ln^{-2}(2/\epsilon)]$, which is only logarithmically smaller than the leading term. In fact, the initial corrections to the leading-order result have been

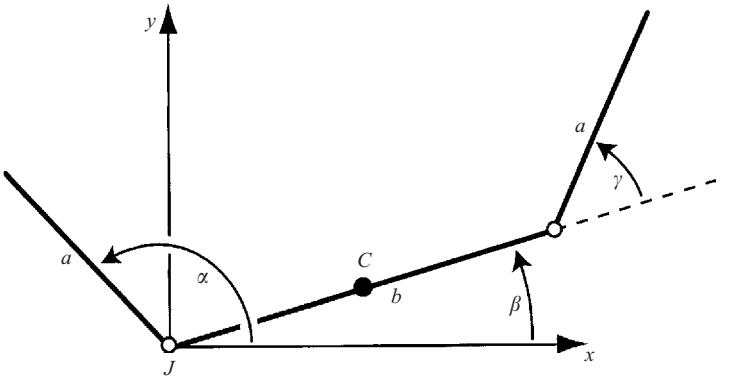

FIGURE 3. Definition diagram for Purcell's three-link swimmer. The left and right arms are of length a, and the middle link is of length b. The active joint is labelled J, and the centre of the middle link is labelled C.

shown by a number of researchers to involve a series in powers of $\ln^{-1}(2/\epsilon)$, and this series may be represented in the form of an integral equation for the local force density (e.g. Hancock 1953; Keller & Rubinow 1976*b*). For the 'scallop' or hinge shown in figure 1(*a*), where the arms are separated by an inner angle of $\delta \equiv (\pi - 2\gamma)$, it may be readily shown that when $\delta \to 0$ and the hinge is nearly closed, the correction to the leading-order approximation for the force density is $O[\ln(\delta)\ln^{-2}(2/\epsilon)]$; this estimate arises from the local viscous drag on one arm caused by the leading-order background flow generated by the other. The leading-order theory presented here is thus valid for all non-zero separation angles in the limit of small slenderness ratios ($\epsilon \to 0$).

We assume in all of our numerical applications that the slenderness ratio ϵ is sufficiently small to justify our use of the leading-order slender-body approximation. Based on the functional dependence of the leading error term given in equation (5), ϵ should then ideally satisfy the condition $|\ln \epsilon| \gg 1$. However, computations using the leading-order approximation have shown reasonable agreement with experimental applications involving thin fibres and filaments at larger slenderness ratios ϵ of the order of 10^{-2} and larger (e.g. Koehler & Powers 2000; Becker & Shelley 2001; and references therein). Thus, from a mathematical point of view, our numerical results are exact in the limit $\epsilon \to 0$, and we further expect them to apply approximately to most practical realizations of Purcell's swimmer.

The methodology developed above is sufficiently general to model a variety of simple objects, where surfaces S_1 and S_2 could, for example, have a continuously varying resistance $\zeta(s)$ corresponding to a non-constant cross-sectional diameter or perhaps a textured surface; in this study, however, we will assume for simplicity that ζ is the same constant for all members of a given linkage. An extension of our approach to multiple joints rotating simultaneously is straightforward, as the corresponding governing equations, in the inertialess limit, may again be derived simply from the assumed slender-body constitutive model plus elementary static force and moment balances that are common in, for example, the field of robotics.

3. Purcell's swimmer

In Purcell's paper on swimming motions at low Reynolds number, the hypothetical three-link swimmer shown in figure 3 was introduced as the simplest "animal" that could swim in the inertialess limit. The linkage consists of a middle link of length

b connected to two arms of equal length a; the arms alternately rotate by an angle of $\pm 2\gamma$ relative to, and in a manner that is symmetric about, the middle link, as indicated in figure 1(b) by the four configurations labelled I to IV. Purcell concluded from symmetry arguments that this two-joint mechanism does not undergo any net rotation over each complete cycle of the four arm strokes, and that each cycle results in a net translation along a straight line, but the direction of this translation and the numerical details of this basic swimming motion have, to the best of our knowledge, never been determined.

Throughout the swimming cycle of Purcell's swimmer, only one joint is active at any one time, and hence the motion may be analysed using the methodology developed in § 2. The grand resistance matrix of equation (4) for Purcell's swimmer was obtained and inverted using the symbolic manipulation software `Maple`, where we non-dimensionalized using a characteristic length scale a, velocity scale $S^{ext}/(\zeta a^2)$, and time scale $\zeta a^3/S^{ext}$; from hereon, all quantities are to be taken as dimensionless, unless specified otherwise. The detailed motion may then be determined by simply integrating forward in time the resulting explicit relations for the generalized velocities.

The general analytical expressions for Purcell's swimmer are too complex to present here; in the limit of zero length of the middle link ($b=0$), however, Purcell's swimmer reduces to the "scallop", and for motion centred about the x-axis as shown in figure 1(a), the non-dimensionalized velocity of the joint is given by

$$(\boldsymbol{U}_J)_x = \frac{\mathrm{d}x_J}{\mathrm{d}t} = \left[\frac{\sin\alpha}{2-\cos^2\alpha}\right]\frac{\mathrm{d}\alpha}{\mathrm{d}t}. \tag{6}$$

This expression may be integrated from $\alpha=\pi/2-\gamma$ to $\alpha=\pi/2$ to obtain the displacement, Δ_x^J, of the joint for the opening motion of the scallop depicted in figure 1(a):

$$\Delta_x^J = \operatorname{arctanh}[(\sin\gamma)/\sqrt{2}]/\sqrt{2}, \tag{7}$$

and the displacement of the centre of each arm of the scallop, Δ_x^C, is equal to $[\Delta_x^J-(\sin\gamma)/2]$. The variations of Δ_x^J and Δ_x^C with the stroke angle $\gamma\in[0,\pi/2]$ are shown in figure 4, highlighting the positive, rightward displacement of both the joint and the arm centres (in fact, the far ends of the arms are displaced in the negative, leftward direction). The reverse path of the motion depicted in figure 1(a) would, of course, be retraced during the closing of the scallop, with no net translation or rotation for reciprocal motions in the inertialess limit.

Returning to the three-link mechanism, the simplest swimmer considered by Purcell, we consider in § 3.1 the detailed motion for a stroke angle of $\gamma=\pi/3$ and a non-dimensionalized middle-link length of $\eta\equiv b/a=2$. This configuration corresponds approximately to that of the swimmer sketched by Purcell (1976). In § 3.2, we treat the small-amplitude arm motion in the limit of small γ, and compare the propulsive dynamics to that of sheets and rods along which plane waves of lateral displacement are propagated. In § 3.3, the large-amplitude arm motion in the limit of $\gamma=\pi$ is discussed.

3.1. *Configuration* $\gamma=\pi/3$ *and* $\eta\equiv b/a=2$

The numerically simulated displacement of Purcell's swimmer with $\gamma=\pi/3$ and $\eta=2$ is depicted in figure 5. The swimmer is centred in the (x,y)-plane, and the four arm motions, labelled 1 to 4, propel it through one complete cycle of configurations, denoted I to IV (as in figure 1b). For Motion 1, which extends over the first quarter of

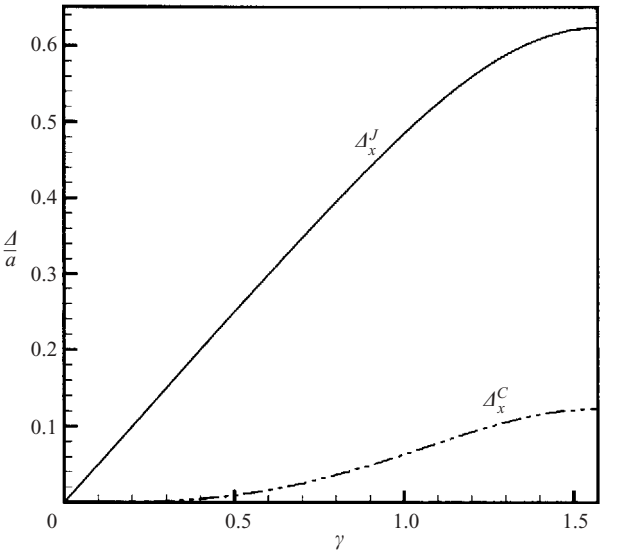

FIGURE 4. The x-displacements Δ_x^J and Δ_x^C of the joint and the arm centre, respectively, versus stroke angle γ for the motion of the scallop depicted in figure 1(a).

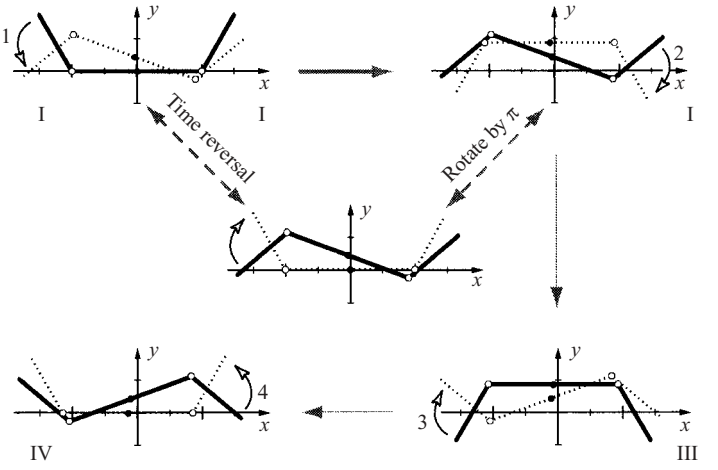

FIGURE 5. The displacement of Purcell's swimmer with $\gamma = \pi/3$ and $\eta = 2$. The motion is centred in the (x, y)-plane, and the four arm strokes labelled 1 to 4 propel the swimmer through one complete cycle of configurations denoted I to IV. In each graph, the starting position is indicated by a solid line, the ending position by a dashed line, and the centre of the middle link by a solid circle. The centre graph indicates the symmetry relation between Motions 1 and 2.

the swimming cycle, the IMSL routine DIVPAG was used to integrate the analytical expressions for the velocities forward in time under constant forcing $S^{ext}\boldsymbol{e}_z$ until the smallest angle between the forcing (left) arm and the middle link equalled its starting value of $|\gamma| = \pi/3$. Motions 2 to 4 are related to the first via symmetry arguments, and do not need to be computed separately. Motion 2, for example, is simply a time-reversal of the first motion rotated by π about the centre C of the middle link, as indicated in the centre graph of figure 5. Denoting the (x, y) displacement of the centre

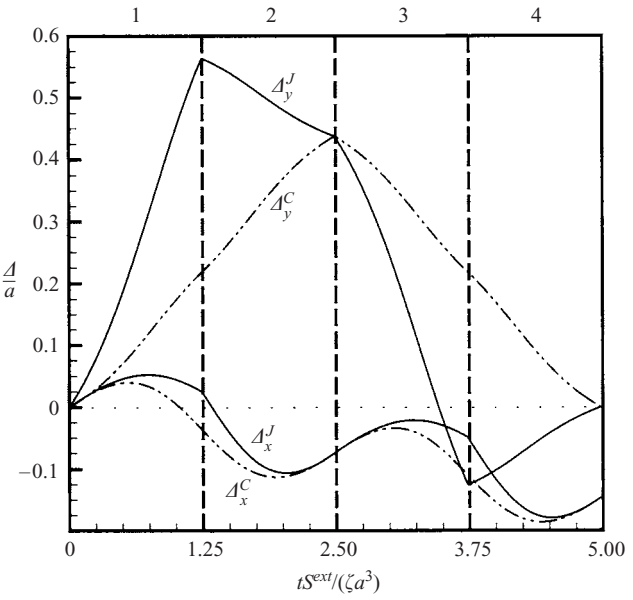

FIGURE 6. The (x, y) displacements (Δ_x, Δ_y) of the centre C and of the left joint J for one swimming cycle (Motions 1 to 4) with parameters $\gamma = \pi/3$ and $\eta = 2$.

of the middle link, C, resulting from the ith arm motion by $(\Delta_{ix}^C, \Delta_{iy}^C)$, such symmetry considerations imply that $\Delta_{1x}^C = \Delta_{2x}^C = \Delta_{3x}^C = \Delta_{4x}^C$, and $\Delta_{1y}^C = \Delta_{2y}^C = -\Delta_{3y}^C = -\Delta_{4y}^C$, so that any rotation of the middle link over one arm stroke is reversed on the subsequent stroke. Hence, over one complete cycle of four arm strokes, Purcell's swimmer will translate purely along a direction given by the middle link of configurations I and III, in this case the x-direction, without rotating. This conclusion was reached previously by Purcell (1976), but the direction and distance of travel was left as an exercise for the reader; as may be seen from the numerically computed configurations in figure 5, the displacement in this case is along the negative x-direction, i.e. to the left. We show below that the swimming direction depends on γ also.

For a more detailed look at the dynamics of Purcell's swimmer with stroke angle $\gamma = \pi/3$ and relative middle-link length $\eta = 2$, we show in figure 6 the (x, y) displacements of the centre C and of the left joint J over the complete cycle considered above. Each of the Motions 1 to 4 is completed in a time of about $1.25\zeta a^3/S^{ext}$, and is associated with a net translation of the centre C of $-0.0368a$ as well as a net rotation of the middle link of $\beta = \pm 0.352$; over one complete cycle, the net speed of translation along the x-direction, denoted V_x, is equal to $-0.0295\ S^{ext}/(\zeta a^2)$. During Motion 1, it is interesting to note that the x-displacement during the first stroke is initially positive for both the joint J and the centre C, and only becomes negative for C near the end of the stroke. Without the insight of numerical simulations, one might intuitively predict that the displacement of the swimmer should be in the positive x-direction, as in the informal discussion of Purcell's swimmer by Castaing (1998).

Based on our simulations, the propulsion of Purcell's swimmer with $\gamma = \pi/3$ and $\eta = 2$, as presented in figures 5 and 6, may be qualitatively explained by the anisotropic nature of the viscous drag on a slender body. The leading-order approximation for the local hydrodynamic force per unit length, given in equation (5), implies that the local resistance of a slender body to fluid motion perpendicular to its centreline is twice

that to motion along its centreline. Keeping this result in mind, we consider Motion 1, as the remaining steps of the swimming cycle follow from the first motion via the symmetry considerations described above. During approximately the first half of the left downward arm stroke, the active joint J and the centre C are displaced up and to the right, similar to the motion of a scallop opening. The displacement to the right, however, is lessened by the far rigid arm, which is least aligned with the horizontal direction at the start of Motion 1, but which progressively becomes more aligned due to the clockwise rotation of the middle link. This clockwise rotation of the middle link proceeds nearly linearly over the entire Motion 1, and thus over the second half of the left arm stroke, where one would intuitively expect displacements that are upward and to the left, the leftward motion is less restrained by the increasingly aligned right rigid arm. By favouring motions that are tangential to it, the far arm acts essentially like a rudder, enhancing the leftward movement of the middle link for small to moderate values of γ less than about $\pi/2$. This argument makes clear that the entire shape of the linkage is important for describing the motion.

Of course the two halves of the left downward arm stroke differ not only by the alignment of the far arm with the horizontal, but also by the cumulative rotation of the middle link itself. For stroke angles γ less than about $\pi/2$, the latter effect turns out to be secondary, and the improved alignment of the far arm over each stroke is responsible for a net translation in the negative x-direction, i.e. to the left. For large-amplitude arm strokes with $\gamma \to \pi$, however, alignment of the far arm with the horizontal in fact worsens over each arm stroke, the rotation of the middle link is the defining feature of the motion, and Purcell's swimmer undergoes a net translation in the opposite direction, i.e. to the right, as shown and discussed later. In the next two subsections, we consider first the small- and then the large-amplitude limits for the stroke angle γ.

3.2. *Small-amplitude motion*

Introducing $\theta \equiv \pi - \alpha$ and expanding (using `Maple` software) the non-dimensionalized solution system represented by equation (4) about the fully extended configuration with $\theta = \beta = \gamma = 0$, we obtain the following expressions for the velocity of the joint J and the angular rotation rates α and β corresponding to Motion 1 (i.e. the initial downward stroke of the left arm):

$$(\boldsymbol{U}_J)_x = -\frac{3}{4}\left[\frac{(\beta-\theta)(\eta+1)+\gamma}{(\eta+1)^2}\right] + O(\gamma^3), \tag{8a}$$

$$(\boldsymbol{U}_J)_y = \frac{3}{2(\eta+1)} + O(\gamma^2), \tag{8b}$$

$$\dot{\alpha} = \frac{3}{4}\left(\frac{\eta+4}{\eta+1}\right) + O(\gamma^2), \tag{8c}$$

$$\dot{\beta} = -\frac{3}{4}\left[\frac{3\eta+4}{(\eta+1)^3}\right] + O(\gamma^2). \tag{8d}$$

Note that as the link ratio $\eta \equiv b/a \to \infty$, $\boldsymbol{U}_J \to \boldsymbol{0}$, $\dot{\alpha} \to 3/4$, and $\dot{\beta} \to 0$. The case $\eta \to 0$, on the other hand, reduces to the scallop considered at the beginning of this section.

Next we determine the time interval t_s, in units of $\zeta a^3/S^{ext}$, required for one stroke. Starting from the initial angles α_i and β_i, with $\gamma = \pi - (\alpha_i - \beta_i)$, the linearized expressions for $\dot{\alpha}(t)$ and $\dot{\beta}(t)$ are integrated with respect to time. From the condition

that the first quarter-cycle ceases when $\alpha - \beta = 2\pi - (\alpha_i - \beta_i)$, it follows that

$$t_s = \left[\frac{8}{3}\frac{\gamma(\eta+1)^3}{(\eta+4)(\eta+1)^2+3\eta+4} + O(\gamma^2)\right]\left(\frac{\zeta a^3}{S^{ext}}\right). \tag{9}$$

Substituting for α and β with $\beta_i = 0$ into $(\boldsymbol{U}_J)_x$ and integrating from $t = 0$ to $t = t_s$, we can obtain the x-displacement over one quarter-cycle, and thus by symmetry the average translational speed V_x, in units of $S^{ext}/(\zeta a^2)$, of the swimmer over the complete swimming cycle:

$$V_x = -\left[\frac{3}{8}\frac{\eta(2\eta+3)\gamma}{(\eta+1)^3(\eta+2)} + O(\gamma^2)\right]\left(\frac{S^{ext}}{\zeta a^2}\right). \tag{10}$$

The translation of a swimmer, starting with $\beta_i = 0$ as depicted in figure 5, is hence to the left for linearized small-amplitude motions about the straightened configuration, regardless of the relative length of the middle link η (with $V_x \to 0$ as $\eta \to 0$ or ∞). To leading order, the translation velocity is linear in the angular amplitude γ for a given forcing of constant magnitude S^{ext} acting alternately at the two joints.

Taylor (1951) and Hancock (1953) studied the propulsion of sheets and rods, respectively, along which plane waves of lateral displacement are propagated. In these studies, the small-amplitude translation velocity is equal to $-\frac{1}{2}\chi k^2 A^2$ plus terms of higher order in kA, where A is the amplitude of the displacement, k is the wavenumber, and χ is the velocity of wave propagation. We can relate our small-amplitude results for Purcell's swimmer to those obtained by Taylor and Hancock by combining equations (9) and (10) to eliminate the forcing S^{ext}:

$$V_x = -\left[\frac{\eta(2\eta+3)}{(\eta+2)[(\eta+4)(\eta+1)^2+3\eta+4]} + O(\gamma)\right]\left(\frac{a}{t_s}\right)\left(\frac{1}{a}\right)^2(\gamma a)^2. \tag{11}$$

This expression for Purcell's swimmer is analogous to the results by Taylor and Hancock for small-amplitude plane-wave propulsion, if we take $A^* = \gamma a$ to be the amplitude of an equivalent wave, $k^* = 1/a$ as an effective wavenumber, and $\chi^* = a/t_s$ as an approximate wave speed that dictates how fast Purcell's swimmer executes each of the four motions of the swimming cycle. Equation (11) for the velocity of Purcell's swimmer can then be written as $V_x = -\frac{1}{2}f(\eta)\chi^* k^{*2} A^{*2}$, but the magnitude of the factor $f(\eta)$ is much smaller than the value of 1 corresponding to the plane-wave result; given an aspect ratio of $\eta = 1$, for example, $f(\eta) = 10/81$.

One can construct a reasonably good visual analogy for the case $\eta = 1$ at any stroke amplitude $\gamma < \pi/2$ by superimposing the end points of the links of Purcell's swimmer in configurations I to IV onto a rightward-travelling sinusoidal wave, as shown in figure 7. The rotation of Purcell's swimmer in the figure is qualitatively similar to what one would expect for its actual motion, suggesting that Purcell's swimmer, at values of $\gamma < \pi/2$ where such an analogy is possible, corresponds approximately to one wavelength of a travelling wave. The rightward-travelling wave of lateral displacement causes a net translation of the undulating rod to the left, and we will show in § 4.1 that Purcell's swimmer, swimming as indicated in figure 1(*b*), will also generally swim to the left for stroke angles of $\gamma \lesssim 2$, supporting the validity of this analogy. As we emphasized in our description of Purcell's swimmer in § 3.1, Hancock (1953) similarly noted the importance of the anisotropy of the fluid drag for a qualitative explanation of the translation of the undulating rod in a direction opposite to that of wave propagation: "... motions of small portions of cylinder normal to themselves tend to be in the backward direction while motions tangential to themselves tend

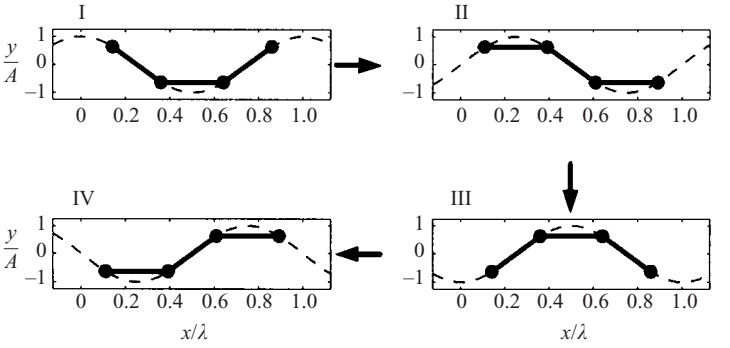

FIGURE 7. Analogy between Purcell's swimmer and plane-wave propagation for an aspect ratio of $\eta = 1$. The end-points of the links in configurations I to IV are superimposed onto a rightward-travelling sinusoidal wave.

to be in the forward direction, resulting in forward motion" (in this case, to the left). This description of the propulsion of the undulating rod cannot be applied directly to Purcell's swimmer, however, due to the latter's relatively large up-and-down displacement perpendicular to the direction of travel (as given in figure 6 for $\gamma = \pi/3$ and $\eta = 2$). The dissimilarity is probably responsible for the poor quantitative agreement between the translation velocity predicted for Purcell's swimmer from this analogy and the true velocity of equation (11) ($f(\eta) \ll 1$). One might further expect Purcell's swimmer to be less efficient than plane-wave propulsion, an argument which we quantify in § 4.1 via the introduction of a new efficiency criterion.

3.3. *Large-amplitude limit*

In the previous two subsections, the arm motions of Purcell's swimmer over configurations I to IV have resulted in a net translation in the negative x-direction, i.e. to the left. It turns out that for large-amplitude arm motions $\gamma \to \pi$, where each arm stroke consists of nearly a full rotation of the arm, our numerical results indicate that the swimmer swims in the opposite direction, i.e. to the right. In the following section, we present a more complete overview of the variation of the net translation velocity with stroke angle γ, while in this subsection we focus on some details of the motion when $\gamma = \pi$ and the arms essentially start and finish on top of the centre link. This limit of course violates slender-body theory, as lubrication forces eventually dominate on close approach of any two surfaces. While our numerical computations are only exact in the limit of small slenderness ratios, our calculated displacements in the full-rotation limit $\gamma = \pi$ will also apply in practical applications where the hydrodynamic interactions are important over only a small part of the configuration space and yield corrections that are negligible relative to the overall motion; the time required to reach this limit, however, would be infinite based on the solution of the Stokes equation for the approach of two locally flat surfaces, and hence we do not discuss propulsive velocities near $\gamma = \pi$.

Additional symmetry arguments, independent of the hydrodynamic approximations, provide intuitive insight into the motion of Purcell's swimmer in the large-amplitude limit. As discussed in § 3.1, the motion of Purcell's swimmer over any one complete arm stroke may be related to that of any of the three other arm strokes via the symmetry features depicted in figure 5. In the full-arm rotation limit $\gamma = \pi$, the motion of each stroke may in turn be broken down into two related motions, and detailed knowledge of any one half-stroke (or one-eighth of the swimming cycle) is

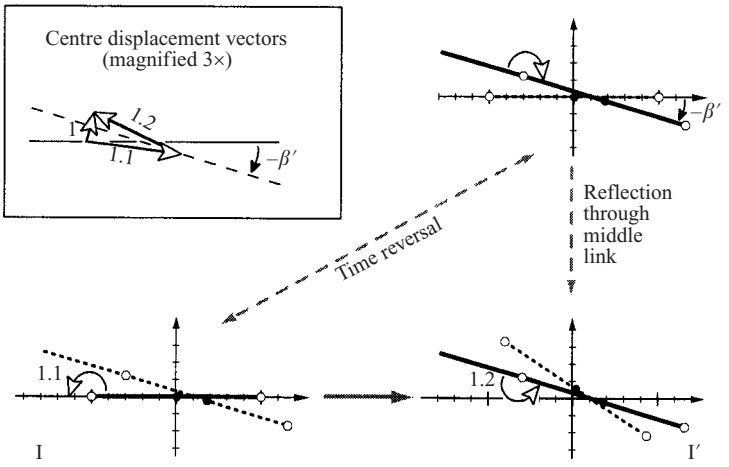

FIGURE 8. Symmetry argument for Purcell's swimmer with $\gamma = \pi$ and $\eta = 2$, showing the decomposition of Motion 1 into the two related Motions 1.1 and 1.2. In each graph, the starting position is indicated by a solid line, the ending position by a dashed line, and the centre of the middle link by a solid circle. Inset shows displacement of centre C. Graphs are based on the slender-body analysis, neglecting lubrication forces and link overlap. Overlap is evident since, for example, in Graph I the starting configuration (solid) appears to be shorter than the opened one (dashed).

sufficient to determine the remaining dynamics. As shown in figure 8 for the case $\eta = 2$, Motion 1 can be decomposed into Motion 1.1, which ends when the arm is in line with the centre link, and Motion 1.2, which is identical to a time-reversal of Motion 1.1 reflected about a line drawn along the centre link half-way through the stroke (configuration I′). Denoting the angle of the centre link in configuration I′ by β', the (x, y) displacements of the centre C occurring over the course of Motion 1.2 are related to those over Motion 1.1 via

$$\begin{bmatrix} \Delta^C_{1.2x} \\ \Delta^C_{1.2y} \end{bmatrix} = \begin{bmatrix} -\cos(2\beta') & -\sin(2\beta') \\ -\sin(2\beta') & \cos(2\beta') \end{bmatrix} \begin{bmatrix} \Delta^C_{1.1x} \\ \Delta^C_{1.1y} \end{bmatrix}. \tag{12}$$

The translation along the x-axis due to Motion 1 is thus given by

$$\Delta^C_{1x} = \Delta^C_{1.1x} + \Delta^C_{1.2x} = [1 - \cos(2\beta')]\Delta^C_{1.1x} - \sin(2\beta')\Delta^C_{1.1y}, \tag{13}$$

and, from § 3.1, the total translation over the four motions of the complete cycle will be equal to $4\Delta^C_{1x}$.

The displacements in the full-rotation limit shown in figure 8 are based on the slender-body analysis described in § 2, and do not account for lubrication forces or the fact that the far arm lies on top of the centre link; we show these results because they are indicative of the displacement of Purcell's swimmer for large-amplitude motions where γ is slightly less than π and where our analysis is appropriate for links of sufficiently small slenderness ratio. Our numerical computations for large-amplitude arm motions indicate that the net translation of Purcell's swimmer over configurations I to IV is to the right, and this result may be confirmed intuitively via the symmetry arguments presented above. From the inset of figure 8, it can be seen that the displacement vector of the centre C under Motion 1.2 is simply the negative of that of Motion 1.1 reflected about the centre link of configuration I′, leading to a net translation over Motion 1 that is to the right and upwards. Intuitively, one

might expect a qualitatively similar picture even if lubrication forces were taken into account at finite values of the slenderness ratio.

While we have not undertaken a more detailed investigation incorporating hydrodynamic interactions, in the full-rotation limit the centre link and the passive folded-in arm would essentially behave as one; realistically, this effective link would have a variable cross-section due to two arms lying side by side, but such variations have a negligible effect on the hydrodynamics at sufficiently small slenderness ratios (Batchelor 1970). Thus, in the limit $\gamma = \pi$, Purcell's swimmer over each stroke is essentially equivalent to a scallop with generally unequal arms. Neglect of the passive arm in our numerical simulations does not alter the qualitative features of the motion shown in figure 8. Corresponding to the case of equal arm lengths ($\eta = 1$) in the full-rotation limit, we have already shown in figure 4 that a scallop opening from the closed to the straight position – Motion 1.1 with neglect of the passive arm – experiences a positive, rightward displacement of the arm centres ($\Delta^C_{1.1x} > 0$); by symmetry, the same rightward displacement occurs as the scallop closes to the opposite side (Motion 1.2), yielding $\Delta^C_{1x} = 2\Delta^C_{1.1x} > 0$ and again supporting our conjecture that, even at practically reasonable values of the slenderness ratio, Purcell's swimmer in the large-amplitude limit should swim in a direction opposite to that for small-amplitude displacements.

4. Discussion

4.1. *Swimming velocity and propulsive efficiency*

The question of which aspect ratio η and stroke angle γ results in the fastest or most efficient Purcell's swimmer depends on how one standardizes the energy-input criteria across different swimmer configurations. For very slow motions under relatively heavy load, muscles and machines generally dissipate much of their energy internally, and their power consumption depends to a large extent on the duration over which they produce a given force or torque, and less on the mechanical work performed on the environment; in the extreme case of zero net motion under load, as occurs when holding a weight out in front of you or when pressing the accelerator just enough to balance a car on a steep incline, no external work is done and all of the expended energy is transformed into heat. For a practical implementation of Purcell's swimmer operating under such conditions where internal energy dissipation is dominant, one possible way to compare swimmer configurations is to let each swimmer exert a constant torque difference S^{ext} over time at either joint for a given arm length a, as was assumed in the previous section. Alternatively, under conditions where internal energy is transformed primarily into mechanical work, one could seek the fastest swimmer such that the mechanical power $\Phi = S^{ext}(t)\omega(t)$, which is dissipated viscously in the fluid, remains constant over time.

In figure 9, we show the net velocity of translation V_x for various η over the complete range of γ for these two energy-input criteria. The slender-body approximation, for a given slenderness ratio ϵ, becomes less and less valid as γ approaches π, and the arms would begin to cross for $\gamma \geqslant \pi - \arccos(\eta/2)$ when $\eta \leqslant 2$. Results for $2 \lesssim \gamma \leqslant \pi$ should be applied with caution to practical realizations of Purcell's swimmer, since hydrodynamic interactions between links may be especially significant (see discussion of equation (5) in § 2); we focus here primarily on smaller stroke amplitudes where the velocity of translation is predominantly negative and the swimming sequence represented by configurations I to IV results in translation to the left. Our numerical results do, however, indicate that the translation velocity will change sign for

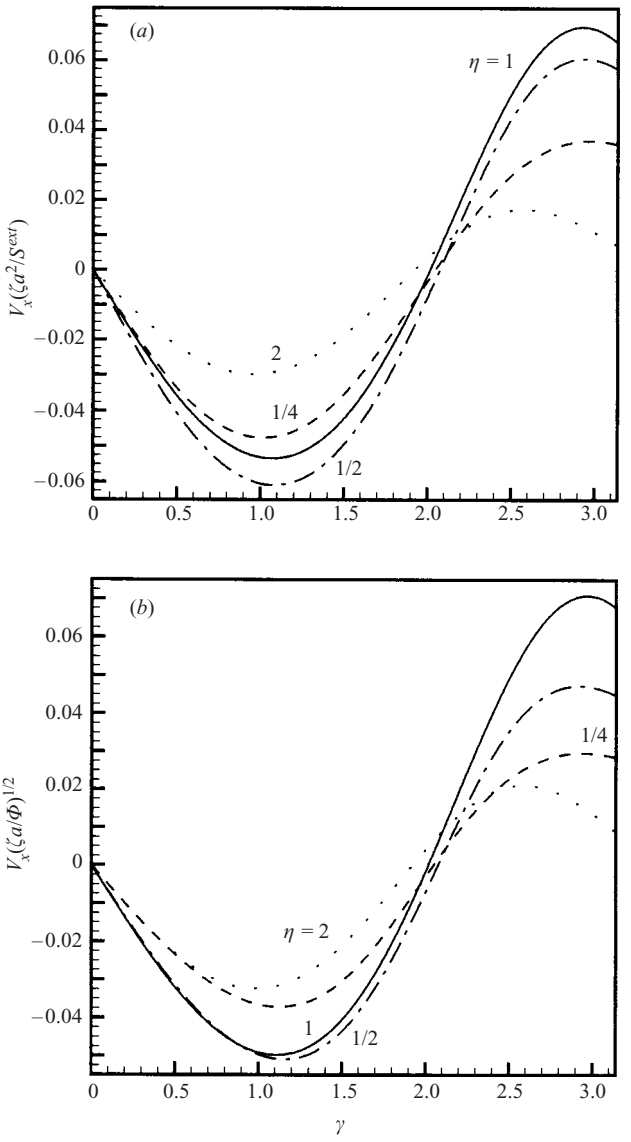

FIGURE 9. The net velocity of translation V_x versus the stroke angle γ for various aspect ratios η: (*a*) constant torque difference S^{ext}, (*b*) constant mechanical power Φ.

large-amplitude motions ($\gamma \gtrsim 2$), and these findings are intuitively confirmed by the symmetry arguments of § 3.3 for the complete-rotation ($\gamma = \pi$) limit shown in figure 8.

For the case of constant torque difference S^{ext} shown in figure 9(*a*), the fastest Purcell's swimmer translating in the negative x-direction has a configuration of $\eta = 0.58$ and $\gamma = 1.09$, with a maximum rotation of the middle link of $\beta_{max} = \pm 0.81$. The motion is qualitatively similar to the one shown in figure 5 for $\eta = 2$, and the optimal swimmer has a translational velocity of $V_x = -0.061 S^{ext}/(\zeta a^2)$. Based solely on the small-amplitude, linear analysis of § 3.2, the optimal aspect ratio would be $\eta = 0.54$.

For the case of constant mechanical power $\Phi = S^{ext}\omega$ shown in figure 9(*b*), the fastest left-moving swimmer has $\eta = 0.69$, $\gamma = 1.14$, $\beta_{max} = \pm 0.80$, and an average translation

velocity of $V_x = -0.053(\Phi/\zeta a)^{1/2}$; the small-amplitude analysis of § 3.2 predicts an optimal aspect ratio of $\eta = 0.76$. Since Φ may be written as some function of instantaneous configuration, g, times $(S^{ext})^2$, where $g = \omega/S^{ext}$ is one component of the mobility matrix obtained from inversion of the resistance matrix in equation (4), the constraint of constant mechanical power may be implemented by simply replacing the forcing S^{ext} in equation (4) by $\pm\sqrt{\Phi/g}$ and integrating as described in § 3 for the case of constant forcing. Alternatively considering Φ as ω^2/g, a quadratic form in angular velocities, it follows immediately from calculus of variations that the total mechanical work performed by Purcell's swimmer while moving between two arbitrary points in configuration space over any time interval $[t_1, t_2]$ is minimized under constant mechanical power, i.e.

$$\min \int_{t_1}^{t_2} \Phi \, \mathrm{d}t \Rightarrow \Phi = \text{constant}. \tag{14}$$

This result is completely analogous to that of conservation of energy in Lagrangian mechanics, where kinetic energy, instead of mechanical power, is of quadratic form in generalized velocities (see Landau & Lifshitz 1976); in the Appendix, we give a proof of equation (14) for the general case of an arbitrary, deformable volume. Thus the fastest swimmer configuration under constant mechanical power will require the least amount of mechanical work to swim a given distance over any fixed time interval.

Our determination of the fastest swimmer under either constant torque difference S^{ext} or constant mechanical power Φ does not allocate greater torque or power to swimmers of larger aspect ratios η, a possibly fair comparison if the length of the middle link is irrelevant to power generation within the swimmer. On the other hand, previous definitions of efficiency for low-Reynolds-number swimming motions have accounted for differences in length by comparing the power required to drag the swimmer at its translation velocity to the average mechanical power generated during the actual swimming motion (see Lighthill 1975 for the undulating sphere, Purcell 1997 for the rotating helix). In this spirit, we define a swimming efficiency $\mathscr{E}$ as the power necessary to pull the straightened swimmer (of length $(\eta + 2)\,a$) along its axis at the average speed of the actual swimmer, V_x, relative to the average mechanical power generated by the actual swimmer to achieve that speed, i.e.

$$\mathscr{E} \equiv \frac{(\eta + 2)\zeta a V_x^2}{\langle \Phi \rangle}. \tag{15}$$

Note that in the numerator of $\mathscr{E}$ we consider the power of pulling the straightened swimmer as opposed to that of dragging some other fixed configuration. The definition allows us to compare Purcell's swimmer to the previously studied motions of the undulating rod and the rotating helix, as it may be applied universally to any swimming slender body.

In figure 10, we plot the efficiency $\mathscr{E}$ versus stroke angle γ under constant mechanical power, a condition which, as noted above, minimizes the average mechanical power required by any given swimmer configuration to achieve some specified net-translation velocity V_x and which thus maximizes the efficiency of that swimmer. The efficiencies given in the figure correspond to the square of the velocities of figure 9(*b*), multiplied by the non-dimensionalized body length $(\eta + 2)$. With this weighting in favour of longer swimmers, the most efficient configuration for leftward propulsion has $\eta = 0.81$, $\gamma = 1.13$, and $\beta_{max} = \pm 0.74$, corresponding to an efficiency of $\mathscr{E}_{max} = 0.00771$. The

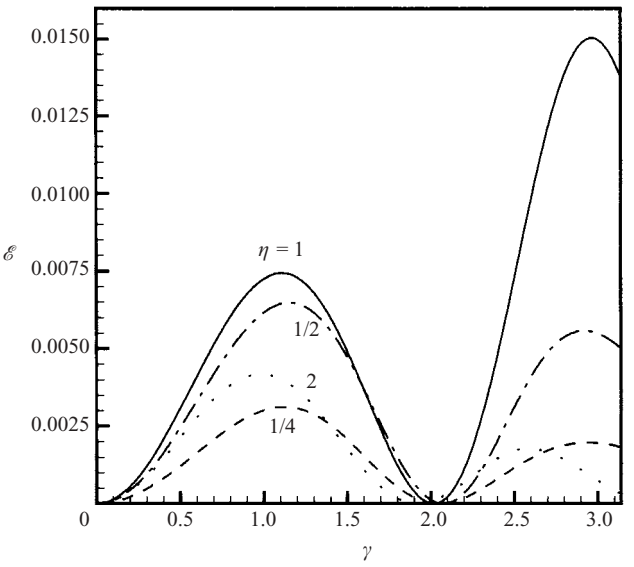

FIGURE 10. The efficiency $\mathscr{E}$ versus the stroke angle γ for various aspect ratios η.

maximum efficiency for rightward propulsion is about twice as large at 0.0155, corresponding to a swimmer undergoing nearly full arm rotations with $\eta = 0.93$, $\gamma = 2.98$, and $\beta_{max} = \pm 2.76$, but this high value of the efficiency may not be realized in practical implementations of Purcell's swimmer due to hydrodynamic interactions between links.

For comparison, our efficiency criterion can be applied to the previously studied swimming motions of the undulating rod and the rotating helix. The former swimmer propagates a plane wave of lateral displacement and the latter two counter-rotating spiral waves of opposite handedness, as depicted in figures 11(*a*) and 11(*b*), respectively, with common wavenumber $k = 2\pi/\lambda$ and wave amplitude A. The velocities of translation V_x are in each case opposite to the velocity of wave propagation χ, and are reproduced in figure 11(*c*) from the analytical results by Hancock (1953) for arbitrarily large wave amplitude (see Hancock 1953, pp. 106 and 117 for plane- and spiral-wave motions, respectively; figure 11(*c*) is equivalent to figure 7 of Hancock but shows a wider range of kA). The velocities may be re-derived most simply from a force balance in the x-direction, whereas the original derivation by Hancock is more complicated due to his inclusion of higher-order non-local hydrodynamic drag. The corresponding values of the efficiency measure $\mathscr{E}$, formally introduced in equation (15), are shown in figure 11(*d*). The undulating rod has a peak efficiency of $\mathscr{E}_{max} = 0.0736$ at $kA = 1.10$, while the helical swimmer, for which we have the simple relation $\mathscr{E} = (kA)^2/[2 + 6(kA)^2 + 4(kA)^4]$, has $\mathscr{E}_{max} = 0.0858$ at $kA = 0.841$. Hence the most efficient rod and helix configurations are more than ten times as efficient as the optimal (left-moving) Purcell's swimmer of figure 10, a result of the relatively large up-and-down movement of Purcell's swimmer relative to its net swimming direction over each cycle.

4.2. *Isotropic drag*

As stated in § 3.1, the local resistance of a slender body to motion perpendicular to its centreline is twice that to tangential motion, and Hancock (1953) emphasized the importance of this anisotropy of the fluid drag to the propulsion of the undulating

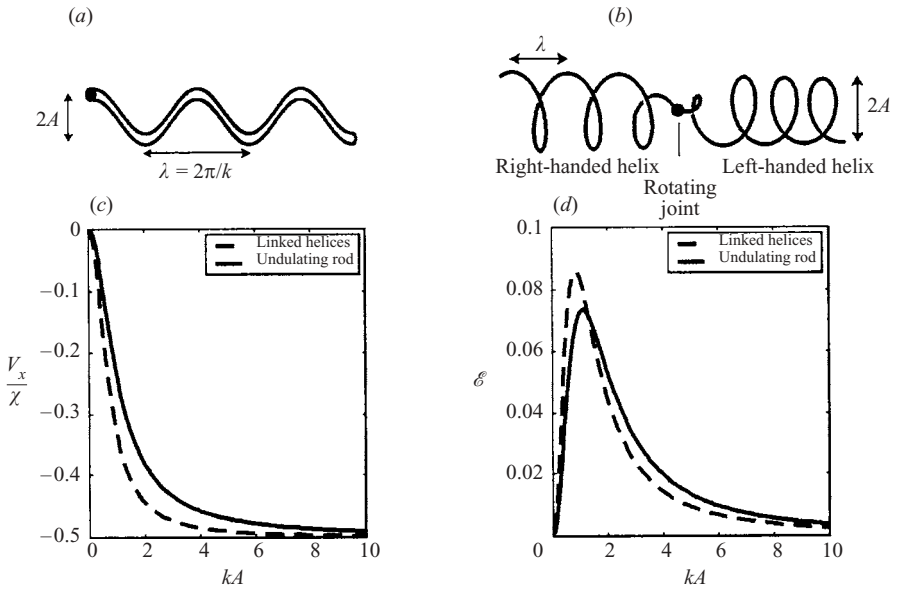

FIGURE 11. Efficiency comparison of the undulating rod and the counter-rotating linked helices with common wavenumber $k = 2\pi/\lambda$ and wave amplitude A: (*a*) definition diagram of the undulating rod, (*b*) definition diagram of the linked helices (an object like this is shown in the film *Low Reynolds Number Flows* by G. I. Taylor), (*c*) translation velocity V_x relative to wave speed χ, (*d*) efficiency $\mathscr{E}$.

rod. The significance of drag anisotropy for more general swimming motions, such as those of Purcell's swimmer, has, to our knowledge, not been discussed in the literature, and some recent studies on the hydrodynamics of slender biological filaments have considered the case where the drag on the filament is locally isotropic. In these studies, the local hydrodynamic force per unit length acting on the filament, $\boldsymbol{f}$, is taken, in the absence of any background flow, as directly proportional to the local filament velocity, $\boldsymbol{U}$, as would be obtained by deleting the term $\boldsymbol{\lambda\lambda}$ in equation (5). For example, Goldstein *et al.* (1998) assumed isotropic drag for the sake of mathematical simplicity in a study of the nonlinear dynamics of curved and twisted rods, while Camalet *et al.* (1999) simply noted from their results that a self-propelled, planar flagellum propagating small-amplitude wave-like disturbances has zero translation speed when the drag is taken as isotropic.

Here we present a simple but general argument proving that under locally isotropic hydrodynamic drag ($\boldsymbol{f} \propto \boldsymbol{U}$), any force-free inextensible swimmer could not change its average position, $\bar{\boldsymbol{r}}$ (or its centre of mass given a constant mass per unit length). Differentiating the average position of an inextensible filament of constant length L with respect to time, we obtain

$$\frac{\mathrm{d}\bar{\boldsymbol{r}}}{\mathrm{d}t} = \frac{1}{L}\frac{\mathrm{d}}{\mathrm{d}t}\int_0^L \boldsymbol{r}(s,t)\,\mathrm{d}s = \frac{1}{L}\int_0^L \frac{\partial \boldsymbol{r}}{\partial t}\,\mathrm{d}s = \frac{1}{L}\int_0^L \boldsymbol{U}\,\mathrm{d}s \propto \int_0^L \boldsymbol{f}\,\mathrm{d}s = \boldsymbol{0}, \qquad (16)$$

where s denotes the arclength along the centreline of the slender body and the last equality follows from the fact that the swimmer is assumed to be force-free. This argument implies that the anisotropy of the slender-body drag is crucial to the propulsion of slender filaments at low Reynolds numbers. It is hence essential that qualitative explanations of the swimming of self-propelled, inextensible, slender

bodies in the inertialess limit, such as the intuitive description of the motion of Purcell's swimmer given in § 3.1, incorporate the inherent drag anisotropy, without which swimming would be impossible.

5. Conclusions

Purcell (1976) introduced the three-link swimmer as the simplest 'animal' or mechanism that could swim at low Reynolds number, but the swimming direction was left as a question for the reader. Our numerical results, based on leading-order slender-body hydrodynamics, show that Purcell's swimmer can travel in either direction along a straight line depending upon the amplitude of the arm motions. For small to moderate stroke angles of the arms ($\gamma \lesssim 2$), Purcell's swimmer is qualitatively similar to approximately one wavelength of an undulating rod propagating a plane-wave disturbance, and the swimming direction is opposite to that of the wave velocity; for larger stroke amplitudes, the direction of net translation reverses. The fastest swimmer configurations under the conditions of constant forcing and of minimum mechanical work were determined. Via a new efficiency criterion, we compared Purcell's swimmer to the undulating rod and the rotating helix; it was shown that the optimal swimmer has an efficiency of only about 0.77%, and so is much less efficient than the optimal undulating rod (7.4%) and the rotating helix (8.6%). Finally, we also proved that under the simplifying assumption of locally isotropic drag, a self-propelled inextensible filament in an otherwise quiescent fluid cannot translate its average position, demonstrating the central importance of drag anisotropy to swimming motions in the inertialess limit.

L.E.B. acknowledges support from DOE grant DE-FG02-88ER25053, and H.A.S. acknowledges grant DAAG 55-97-1-0114 from the Army Research Office as well as grant ECS-0004030 from the National Science Foundation. H.A.S. thanks A. Samuel for numerous helpful discussions about swimming micro-organisms. We thank R. Day, T. Squires and H. Berg for discussions.

Appendix. Minimum mechanical work

In this Appendix, we consider a continuous, freely deformable volume with bounding surface S that evolves, in an otherwise quiescent fluid under the inertialess (zero-Reynolds-number) regime, between two arbitrary surface positions $\boldsymbol{x}_1$ and $\boldsymbol{x}_2$ in a given time interval $[t_1, t_2]$. We then demonstrate that among all possible displacement strategies, the one that minimizes the total mechanical work must have constant mechanical power throughout the motion.

Let each point of the surface be mapped onto a pair of Lagrangian marker coordinates α_1 and α_2, so that the position on the surface is described by the position vector $\boldsymbol{x} = \boldsymbol{x}(\alpha_1, \alpha_2, t)$. Consider one particular evolution $\boldsymbol{x} = \hat{\boldsymbol{x}}$ of the surface between $\hat{\boldsymbol{x}}(t = t_1) = \boldsymbol{x}_1$ and $\hat{\boldsymbol{x}}(t = t_2) = \boldsymbol{x}_2$. Based on this motion, define a configuration space $\hat{\boldsymbol{x}}(\alpha_1, \alpha_2, q)$, $q \in [t_1, t_2]$, where the variable q parameterizes this particular sequence of surface shapes. This configuration space may be traversed by the volume in time at different rates, as specified by the function $q(t)$ with $q(t = t_1) = t_1$ and $q(t = t_2) = t_2$. We will show that for such a configuration space corresponding to any one of all possible spatial evolutions of the surface between $\boldsymbol{x}_1$ and $\boldsymbol{x}_2$, the total mechanical work is minimized by choosing the function $q(t)$ such that the mechanical power is constant.

The velocity at any point of the surface traversing a given configuration space $\hat{\boldsymbol{x}}(\alpha_1, \alpha_2, q)$ is given by

$$\boldsymbol{u} = \frac{\partial \boldsymbol{x}}{\partial t} = \frac{\partial \hat{\boldsymbol{x}}(\alpha_1, \alpha_2, q)}{\partial q}\dot{q}, \tag{A 1}$$

where $\dot{q} = \mathrm{d}q/\mathrm{d}t$, and hence the velocity may be considered as some known function of q times $\dot{q}$. The local force per unit area, $\boldsymbol{n}\cdot\boldsymbol{\sigma}$, acting on any point of the surface at time t may, by the linearity of the quasi-steady Stokes equations (3*a*) and (3*b*), be written as a surface integral of the velocities at time t multiplied by an instantenous Green's function (e.g. Kim & Karilla 1991), an expression which may also be transformed via $t = t(q)$ into a function of q multiplied by $\dot{q}$. Thus, the mechanical power, Φ, taken as a function of $q(t)$ and $\dot{q}(t)$, is quadratic in $\dot{q}$:

$$\Phi = \int_{S(t)} \boldsymbol{n}\cdot\boldsymbol{\sigma}\cdot\boldsymbol{u}\,\mathrm{d}S = [F(q)\dot{q}]^2, \tag{A 2}$$

where the function $F(q)$ depends only upon the surface shape at time $t(q)$.

The total mechanical work, W, performed in traversing any given configuration space may be written as

$$W = \int_{t_1}^{t_2} \Phi\,\mathrm{d}t = \int_{t_1}^{t_2} [F(q)\dot{q}]^2\,\mathrm{d}t, \tag{A 3}$$

and it follows immediately from the calculus of variations that this integral is minimized when the integrand, the mechanical power Φ, is constant (e.g. Landau & Lifshitz 1976). Alternatively, application of the Schwartz inequality for functions (e.g. Arfken 1985) yields

$$W = \int_{t_1}^{t_2} [F(q)\dot{q}]^2\,\mathrm{d}t \geqslant \frac{1}{t_2 - t_1}\left[\int_{t_1}^{t_2} F(q)\dot{q}\,\mathrm{d}t\right]^2 = \frac{1}{t_2 - t_1}\left[\int_{t_1}^{t_2} F(q)\,\mathrm{d}q\right]^2, \tag{A 4}$$

where the last integral, obtained via application of the chain rule, is equal to some constant that is independent of $\dot{q}$, the rate at which the configuration space for a given surface-shape evolution is traversed. Hence regardless of the choice of $q(t)$, for any particular configuration space the total mechanical work is always greater than or equal to this constant. Since our form of the Schwartz inequality becomes an equality only when the integrand of the work integral, the mechanical power Φ, is also constant, the minimum mechanical work for each possible spatial evolution sequence of the surface is thus achieved by choosing $\dot{q}$ such that

$$\Phi = [F(q)\dot{q}]^2 = \text{constant}. \tag{A 5}$$

The above proof was designed to avoid reference to results from the calculus of variations. An alternative would be to, for example, expand the dependence of the surface position $\boldsymbol{x}$ on the Lagrangian markers α_1 and α_2 in terms of orthogonal polynomials with time-dependent mode amplitudes, to then write the mechanical power Φ as a quadratic form in time derivatives of mode amplitudes, and finally to use the calculus of variations (e.g. Arfken 1985) to conclude that Φ must be constant. The latter approach would also lead, as an intermediate step, to the Euler equations governing the extrema of the work integral over all possible surface evolutions.

REFERENCES

Ajdari, A. & Stone, H. A. 1999 A note on swimming using internally generated traveling waves. *Phys. Fluids* **11**, 1275–1277.

Arfken, G. 1985 *Mathematical Methods for Physicists*. Academic.

Batchelor, G. K. 1970 Slender-body theory for particles of arbitrary cross-section in Stokes flows. *J. Fluid Mech.* **44**, 419–440.

Becker, L. E. & Shelley, M. J. 2001 Instability of elastic filaments in shear flow yields first-normal-stress differences. *Phys. Rev. Lett.* **87**, art. 198301.

Berg, H. C. 2002 How Spiroplasma might swim. *J. Bacteriol.* **184**, 2063–2064.

Blake, J. R. 1971 A spherical envelope approach to ciliary propulsion. *J. Fluid Mech.* **46**, 199–208.

Camalet, S., Jülicher, F. & Prost, J. 1999 Self-organized beating and swimming of internally driven filaments. *Phys. Rev. Lett.* **82**, 1590–1593.

Castaing, B. 1998 An introduction to hydrodynamics. In *Hydrodynamics and Nonlinear Instabilities* (ed. C. Godrèche & P. Manneville). Cambridge University Press.

Childress, S. 1981 *Mechanics of Swimming and Flying*. Cambridge University Press.

Goldstein, R. E., Powers, T. R. & Wiggins, C. H. 1998 Viscous nonlinear dynamics of twist and writhe. *Phys. Rev. Lett.* **80**, 5232–5235.

Hancock, G. J. 1953 The self-propulsion of microscopic organisms through liquids. *Proc. R. Soc. Lond.* A **217**, 96–121.

Happel, J. & Brenner, H. 1965 *Low Reynolds Number Hydrodynamics*. Prentice-Hall.

Hill, N. A., Pedley, T. J. & Kessler, J. O. 1989 Growth of bioconvection patterns in a suspension of gyrotactic micro-organisms in a layer of finite depth. *J. Fluid Mech.* **208**, 509–543.

Hinch, E. J. 1972 Note on the symmetries of certain material tensors for a particle in Stokes flow. *J. Fluid Mech.* **54**, 423–425.

Iddan, G., Meron, G., Glukhovsky, A. & Swain, P. 2000 Wireless capsule endoscopy. *Nature* **405**, 417.

Ishiyama, K., Sendoh, M., Yamazaki, A., Inoue, M. & Arai, K. I. 2001*a* Swimming of magnetic micro-machines under a very wide range of Reynolds number conditions. *IEEE Trans. Magnet.* **37**, 2868–2870.

Ishiyama, K., Sendoh, M., Yamazaki, A. & Arai, K. I. 2001*b* Swimming micro-machine driven by magetic torque. *Sensor Actuat. A-Phys.* **91**, 141–144.

Keller, J. B. & Rubinow, S. I. 1976*a* Swimming of flagellated microorganisms. *Biophys. J.* **16**, 151–170.

Keller, J. B. & Rubinow, S. I. 1976*b* Slender-body theory for slow viscous flow. *J. Fluid Mech.* **75**, 705–714.

Kim, S. & Karrila, S. J. 1991 *Microhydrodynamics: Principles and Selected Applications*. Butterworth-Heinemann.

Koehler, S. A. & Powers, T. R. 2000 Twirling elastica: Kinks, viscous drag and torsional stress. *Phys. Rev. Lett.* **85**, 4827–4830.

Landau, L. D. & Lifshitz, E. M. 1976 *Mechanics*. Pergamon.

Lighthill, J. 1975 *Mathematical Biofluiddynamics*. Regional Conference Series in Applied Mathematics, vol. 17, SIAM.

Lighthill, J. 1996 Helical distribution of stokeslets. *J. Engng Maths* **30**, 35–78.

Pedley, T. J. & Kessler, J. O. 1987 The orientation of spheroidal microorganisms swimming in a flow field. *Proc. R. Soc. Lond.* B **231**, 47–70.

Phan-Thien, N., Tran-Cong, T. & Ramia, M. 1987 A boundary-element analysis of flagellar propulsion. *J. Fluid Mech.* **184**, 533–549.

Purcell, E. M. 1977 Life at low Reynolds number. *Am. J. Phys.* **45**, 3–11.

Purcell, E. M. 1997 The efficiency of propulsion by a rotating flagellum. *Proc. Natl Acad. Sci.* **94**, 11307–11311.

Shapere, A. & Wilczek, F. 1989*a* Geometry of self-propulsion at low Reynolds number. *J. Fluid Mech.* **198**, 557–585.

Shapere, A. & Wilczek, F. 1989*b* Efficiencies of self-propulsion at low Reynolds number. *J. Fluid Mech.* **198**, 587–599.

Stone, H. A. & Samuel, A. D. T. 1996 Propulsion of microorganisms by surface distortions. *Phys. Rev. Lett.* **77**, 4102–4104.

Taylor, G. I. 1951 Analysis of the swimming of microscopic organisms. *Proc. R. Soc. Lond.* A **209**, 447–461.

Wiggins, C. H. & Goldstein, R. E. 1998 Flexive and propulsive dynamics of elastica at low Reynolds numbers. *Phys. Rev. Lett.* **80**, 3879–3882.